Article

Indirect-to-direct bandgap transition in GaP semiconductors through quantum shell formation on ZnS nanocrystals

Hongjoo Shin[1,4], Doosun Hong[2,4], Hyunjin Cho[1], Hanhwi Jang ®[1], Geon Yeong Kim ®[1], Kyeong Min Song ®[1], Min-Jae Choi ®[3] ✉, Donghun Kim ®[2] ✉ & Yeon Sik Jung ®[1] ✉

Although GaP, a III-V compound semiconductor, has been extensively utilized in the optoelectronic industry for decades as a traditional material, the inherent indirect bandgap nature of GaP limits its efficiency. Here, we demonstrate an indirect-to-direct bandgap transition of GaP through the formation of quantum shells on the surface of ZnS nanocrystals. The ZnS/GaP quantum shell with a reverse-type I heterojunction, consisting of a monolayer-thin GaP shell grown atop a ZnS core, exhibits a record-high photoluminescence quantum yield of 45.4% in the violet emission range (wavelength = 409 nm), validating its direct bandgap nature. Density functional theory calculations further reveal that ZnS nanocrystals, as the growth platform for GaP quantum shells, play a crucial role in the direct bandgap formation through hybridization of electronic states with GaP. These findings suggest potential for achieving direct bandgaps in compounds that are constrained by their inherent indirect energy gaps, offering a strategy for tailoring energy structures to significantly improve efficiencies in optoelectronics and photovoltaics.

More efficient energy harnessing or conversion from various sources represents a crucial challenge across multiple engineering disciplines. In this context, materials for light-emitting and photovoltaic applications offer particular advantages in optical and electrical performance, primarily when they possess a direct bandgap, which eliminates energy loss due to momentum transfer[1–4]. Interestingly, some materials, such as mono- or few-layer transition metal dichalcogenides[5], have been demonstrated to transition from their inherent indirect bandgap to a direct one. Due to their unique properties, efforts to induce indirect-to-direct bandgap transitions are growing across both scientific and practical domains. Current research approaches include strain application[6,7], compositional modifications[2,8,9], and quantum confinement[5,10]. Nevertheless,

strategies based on strong substrate-layer interactions are notably scarce in the existing literature.

Gallium phosphide (GaP) is a representative III-V indirect-bandgap semiconductor with a zinc blende crystal structure, where the conduction band minimum (CBM) and the valence band maximum (VBM) are located at different k points[3]. Despite its indirect bandgap nature, GaP has been extensively utilized in optoelectronic devices such as solid-state light-emitting diodes (LEDs) for over half a century[11], primarily due to its economic advantages and adequate optical properties. However, its inherent limitation of having an indirect bandgap results in considerably low light conversion efficiency[12,13]. Consequently, extensive simulations have been conducted to explore conditions that could allow GaP to exhibit a direct bandgap, thereby

[1]Department of Materials Science and Engineering, Korea Advanced Institute of Science and Technology, 291 Daehak-ro, Yuseong-gu, Daejeon 34141, Republic of Korea. [2]Computational Science Research Center, Korea Institute of Science and Technology, 14-gil 5, Hwarang-ro, Seongbuk-gu, Seoul 02792, Republic of Korea. [3]Department of Chemical and Biochemical Engineering, Dongguk University, Pildong-ro 1-gil, Jung-gu, Seoul 04620, Republic of Korea. [4]These authors contributed equally: Hongjoo Shin, Doosun Hong. ✉e-mail: minjae.choi@dgu.ac.kr; donghun@kist.re.kr; ysjung@kaist.ac.kr

enhancing its optical and electrical utilization. The computational studies highlighted two viable methods: (i) GaP quantum dots (QDs) with diameters less than 1.5-2 nm[14,15], or (ii) GaP with metastable wurtzite structure, rather than its conventional zinc blende structure[3,16]. Furthermore, a recent study suggests that (iii) the combination of a small-diameter GaP with an anion-rich surface is the key to achieving direct bandgap characteristics[12].

Nevertheless, each of these strategies faces practical or theoretical challenges. While many efforts have been made to experimentally demonstrate direct bandgap GaP QDs using strategy (i), their extremely small size presents significant challenges in synthesis and purification[14,17,18]. For this reason, previous studies have encountered difficulties in eliminating the influence of organic compounds or byproducts, which may compromise the purity and performance of the samples[19]. Due to these limitations, GaP QDs have been used primarily for two purposes: either to mitigate lattice mismatch between indium phosphide (InP) cores and zinc sulfide (ZnS) shells[20], or to increase the bandgap of InP QDs through the formation of indium gallium phosphide (InGaP) alloys[9,21]. However, no experimental results have yet shown band-edge emission from GaP with a direct energy gap.

In contrast, while standard direct bandgap semiconductors exhibit recombination between the heavy hole (Γ_7) and bright conduction band (Γ_9), wurtzite GaP in strategy (ii) forms a pseudo-direct bandgap between the heavy hole (Γ_7) and the dark conduction band (Γ_8)[22]. This leads to poor band-to-band emission due to forbidden transitions governed by optical selection rules[23,24]. In strategy (iii), a P (anion)-rich surface can theoretically induce direct bandgap characteristics, but their anionic surface acts as hole traps[25,26], thereby reducing the photoluminescence (PL) quantum yield. Given these complexities in achieving direct bandgap GaP, a new approach is required to address the limitations of existing strategies, and henceforth pave the way for advanced high bandgap optoelectronic applications.

Here, we report on the colloidal synthesis of direct bandgap GaP quantum shells (QSs) on the surface of a ZnS core with a reverse-type I structure, in which generated charge carriers are confined within the shell. We discovered that the ZnS nanocrystal (NC) template plays a crucial role in forming direct-bandgap GaP QSs, as evidenced by density functional theory (DFT) calculations; ZnS forms a hybrid state with GaP that initiates an indirect-to-direct bandgap transition in GaP. As a result, the GaP QSs on ZnS cores exhibit strong band-edge emission at a wavelength of 409 nm, whereas the GaP QDs present negligible light-emitting characteristics. Our ZnS/GaP QSs achieve a photoluminescence quantum yield (PLQY) of up to 45.4% at 409 nm, which represents the highest deep-blue (violet) emitting characteristics among III-V-based semiconductors to date[27–31] (Supplementary Table 1 and Supplementary Fig. 1). Furthermore, the ZnS/GaP QSs exhibit remarkable long-term stability, as evidenced by a PLQY that is maintained at levels (-107%) commensurate with those observed immediately after the purification, even after a period of 207 days.

Results

The structure of the synthesized ZnS/GaP QS is depicted in Fig. 1a, where it is grown as a monolayer shell on a ZnS core. We selected ZnS as the optimal core material for the growth and manifestation of PL properties for GaP QS for several reasons. First, the lattice parameter (5.41 Å) of ZnS[20], which is very close to that (5.45 Å)[32] of GaP, makes it favorable to form a GaP layer with minimal lattice distortion. Second, in terms of energy structures, ZnS possesses a larger bandgap compared to GaP, with its CBM and VBM levels positioned outside those of GaP. This reverse-type I structure confines electrons/holes in the shell and allows for their direct recombination. Importantly, as will be shown in this study, ZnS forms a hybrid state with GaP at the CBM, facilitating a direct bandgap formation at the Γ point that would be otherwise unattainable with GaP alone. The difference in PL between the conventional GaP QDs and the ZnS/GaP QSs can be visually confirmed under a UV lamp (Fig. 1b).

X-ray diffraction (XRD) analysis revealed that both the synthesized ZnS core nanocrystals and ZnS/GaP QSs exhibit a zinc blende[20] crystal structure (Fig. 1c). This result suggests that the formation of GaP QSs on ZnS does not induce lattice distortion in ZnS owing to their similar lattice parameters. The XRD data also confirmed that there is no crystal structure of oxides and phosphates such as Ga_2O_3 or $GaPO_4$ are not formed[33], consistent with the design shown in Fig. 1a.

To elucidate the reverse-type I energy level alignment in ZnS/GaP QSs, the electron cut-off and valence band maximum regions were examined using ultraviolet photoelectron spectroscopy (UPS) measurements (Fig. 1d, e). The energy band structure of the ZnS/GaP QSs is depicted in Fig. 1f, where the band positions relative to the vacuum level were determined based on data from both UPS measurements and optical bandgap analysis data. The CBM of GaP is positioned below that of ZnS, while the VBM of GaP is located above that of ZnS, providing experimental evidence for the reverse-type I structure, where exciton recombination occurs within the GaP QSs. However, due to the oxophilic nature of Ga[31] and P[34], it is also crucial to demonstrate that the characteristics of the synthesized product are derived solely from GaP itself, rather than from oxide or phosphate compounds. The synthesized products in this study exhibited a significantly smaller bandgap than that of bulk Ga_2O_3 (4.9 eV)[31] or bulk $GaPO_4$ (4.4 eV)[35].

To further verify the GaP QS formation on ZnS, we carried out scanning transmission electron microscopy (STEM) and transmission electron microscopy (TEM) analyses (Fig. 2a and Supplementary Fig. 2). The ZnS core exhibited a diameter of 3.54 nm, while the ZnS/GaP QSs synthesized at 200 °C, 250 °C, and 300 °C for 1 h displayed diameters of 3.77 nm, 3.97 nm, and 4.02 nm, respectively (Fig. 2b). The diameter of the ZnS/GaP QSs increased proportionally with the reaction temperature, reaching a saturation point at 300 °C. This indicates that higher temperatures promote the enhanced growth of the GaP shell on the ZnS core. The d-spacing of GaP planes, which are likely to grow on ZnS considering the XRD pattern shown in Fig. 1c, are 0.31, 0.19, and 0.16 nm for (111), (220), and (311), respectively[14,36]. Based on these d-spacing of GaP planes, we reasoned that an increase in the diameter of ZnS/GaP QSs reflects an increasing surface coverage of the GaP shell on the ZnS surface, and eventually, a monolayer-thin GaP shell is formed. This was further supported by inductively coupled plasma mass spectrometry (ICP-MS) measurements, which show that the amount of elemental Ga and P increases with an increase in synthesis temperature (Fig. 2c). The elemental composition of the ZnS/GaP QS was also confirmed through energy-dispersive X-ray mapping, as presented in Supplementary Fig. 3, thus verifying the presence of Zn, S, Ga, and P.

We investigated the absorption spectra of ZnS/GaP QSs to provide important insights into their core-shell structure. For all samples, the scales of the absorption spectra were adjusted by setting an absorbance of 1 at the excitonic absorption peak (or shoulder) of the ZnS core to facilitate easier comparison among samples. The absorption spectra of the ZnS/GaP QSs can be divided into two parts: absorption in the 300−390 nm range is primarily influenced by the GaP shell, while absorption below 300 nm originates from the ZnS core (Fig. 2d, e). The absorption of ZnS/GaP QSs in the 300−390 nm range consistently increased with either a rising synthesis temperature or an extended synthesis time for GaP growth. This observation is in good agreement with the TEM and ICP-MS results, which indicate that the coverage of the GaP shell can be controlled through synthesis conditions.

A similar trend in emission properties was also observed; the PL intensity of ZnS/GaP QSs increases as the GaP shell grows (Fig. 2e inset, Fig. 2f, Supplementary Figs. 4 and 5). It should be noted that the PL peak position and full width at half maximum (FWHM) remain constant at 409 nm and 68 nm, respectively, whereas the PL intensity shows a significant difference. This confirms that the GaP shell grows as a monolayer on the ZnS surface, resulting in changes in absorption and PL intensity without altering the peak position or FWHM. Moreover, these absorption spectra and the FWHM of PL characteristics are not
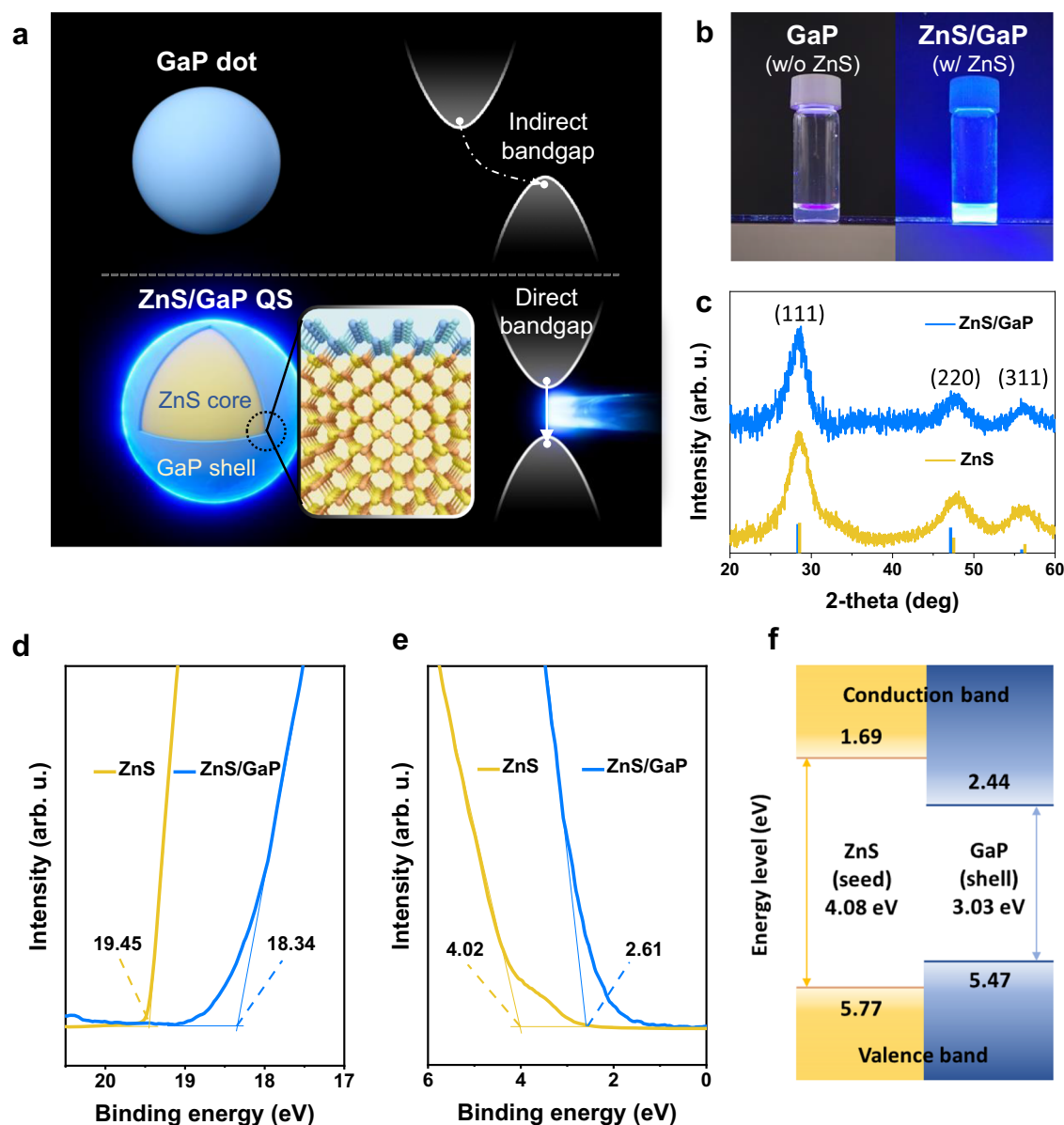
Fig. 1 | Structural features of ZnS/GaP QSs. a The schematic of a GaP dot and a ZnS/GaP QS. **b** A photograph of GaP in the absence and presence of a ZnS core, taken under a 365 nm excitation UV lamp. **c** X-ray diffraction (XRD) patterns of ZnS nanocrystals and ZnS/GaP QS. The vertical lines indicate zinc blende ZnS (yellow) and GaP (blue) diffraction patterns. **d** The spectra of the secondary electron cut-off, and (**e**), the valence band region from UPS measurements. **f** The energy band diagram of GaP QS based on UPS results and optical bandgap. A reverse-type I energy structure was confirmed.

typically observed in Ga_2O_3, which is known for its wide bandgap and broad FWHM (>100 nm) due to donor-acceptor PL[37].

We note that the sequence of shell formation is important for growing the GaP layer. We compared the ZnS/GaP QSs prepared by two different sequences: the injection of Ga precursors first followed by the injection of P precursors (referred as Ga first), and the injection of P precursors first followed by the injection of Ga precursors (referred as P first). Both QSs exhibited similar absorption spectra, showing shoulders at 356 nm and 372 nm due to GaP absorption (Supplementary Fig. 6). However, the ZnS/GaP QSs prepared by the P first method showed higher absorbance intensity in the GaP absorption region compared to QSs prepared by the Ga first method. Similarly, the QSs prepared by the P first method exhibited higher PL intensity compared to the QSs prepared by the Ga first method. These results suggest that a greater amount of GaP was formed in the P first process compared to the Ga first process, which can be explained by the cation-rich nature of the ZnS nanocrystals[38].

To characterize the emission properties quantitatively, we performed PLQY measurements of ZnS/GaP QSs depending on the GaP growth conditions. At a synthesis temperature of 250 °C, the PLQY consistently increased with extended GaP growth time and reaches a saturated PLQY of 45.4% after 60 min (Fig. 2g and Supplementary Table 2). However, when the growth time exceeded 1 h, the PLQY saturated and ceased to increase. For instance, in the case of a 90 min reaction at 250 °C, a PLQY of 43.4% was observed. This data indicates that, with a 1 h reaction time, GaP shell has already formed as a monolayer on the surface of ZnS, and no further GaP shell growth occurs, even with longer reaction times. Additionally, the GaP QSs synthesized at 250 °C, the condition for the best PLQY, exhibited exceptional long-term stability, recording 1.07 times higher PLQY even 207 days later, as shown in Supplementary Fig. 7.

We synthesized a thicker GaP shell on ZnS/GaP to clarify that all these optical properties originate from the GaP monolayer. The TEM image of the ZnS/GaP thick shell showed that the thickness of the GaP layer is ~0.39 nm, which is thicker than the ~0.22 nm of the ZnS/GaP QSs
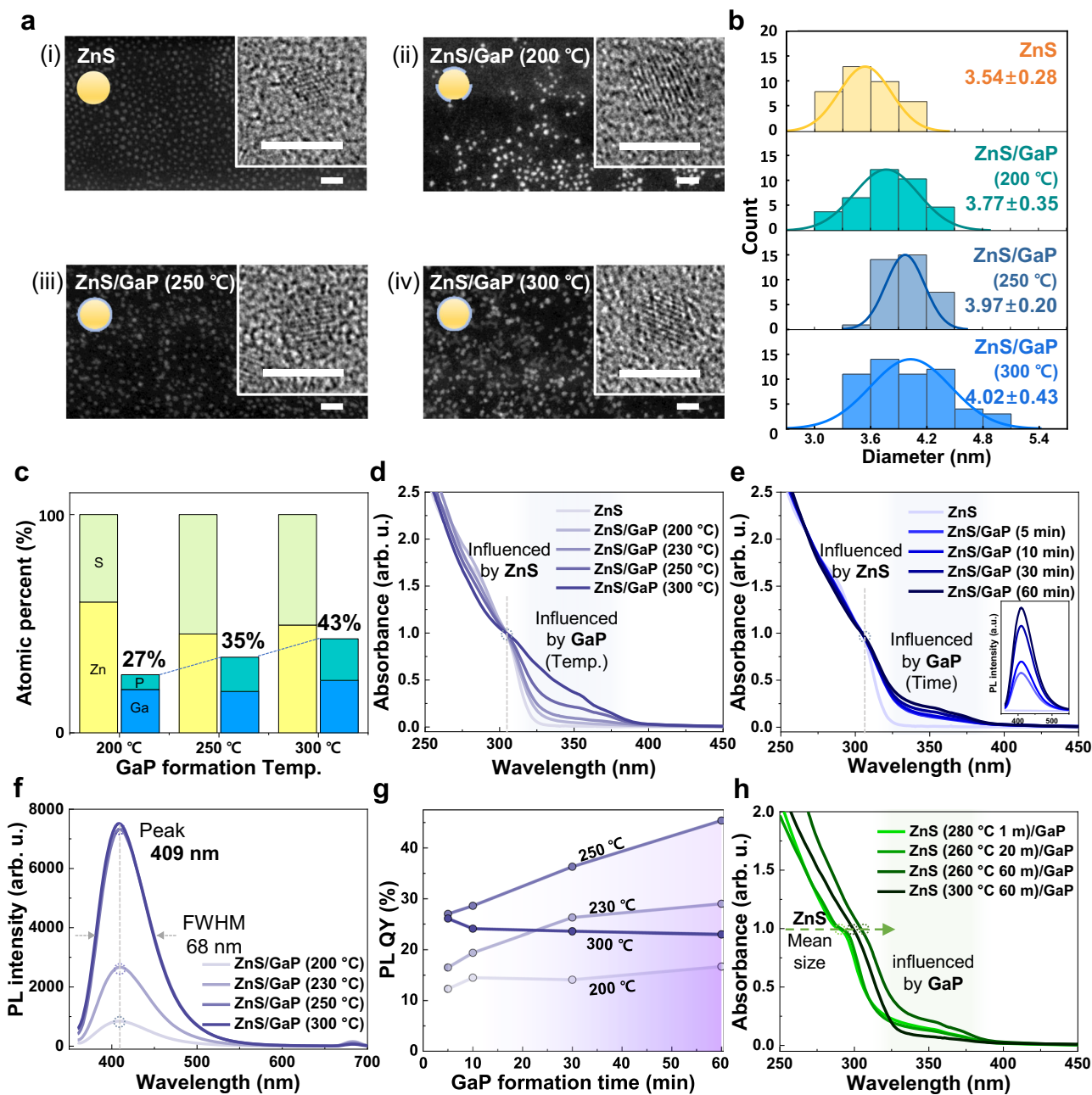
Fig. 2 | Optical characteristics of ZnS/GaP QS. a STEM image showing (i) ZnS core and ZnS/GaP QSs synthesized at temperatures of (ii) 200 °C, (iii) 250 °C, and (iv) 300 °C (scale bar: 20 nm). The inset displays a high-resolution TEM image (scale bar: 5 nm). **b** Particle size histograms fitted with Gaussian curves, based on the STEM images. **c** Quantitative analysis of the Ga-to-P ratio relative to the Zn-to-S ratio, as a function of GaP shell formation temperature, obtained using ICP-MS. **d** Absorption spectra of ZnS core and ZnS/GaP QSs as a function of GaP shell formation temperature. The dotted line and circle indicate the absorption shoulder of ZnS core. **e** Absorption spectra as a function of GaP shell formation

time. The inset in (**e**) displays the photoluminescence (PL) spectra for each sample. The inset PL spectra are also shown in the Supplementary Fig. 4c(ii). **f** PL spectra of ZnS/GaP QSs, measured as a function of GaP shell formation temperature. **g** Photoluminescence quantum yield (PLQY) of ZnS/GaP QSs as a function of both GaP shell formation time and temperature. **h** Absorption spectra of ZnS/GaP QSs as a function of ZnS core conditions. Unless otherwise noted, the default synthesis conditions for the ZnS cores are 260 °C for 60 min, and for the GaP shells, 250 °C and a synthesis time of 60 min.

(Supplementary Fig. 8). ICP-OES measurements revealed that the ratio of the GaP shell to the ZnS core increased significantly from 35% in the ZnS/GaP QSs to 89% in the ZnS/GaP thick shells (Supplementary Fig. 10). Based on the combined ICP-OES and TEM data, 2–3 layers of the GaP shell formed in the ZnS/GaP thick shells, whereas the ZnS/GaP QSs have a monolayer of GaP shell. XPS analyses also showed that the only difference between the ZnS/GaP thick shells and the ZnS/GaP QSs was an increase in the peaks corresponding to Ga-P bonds in the Ga 2*p* and P 2*p* regions (Supplementary Fig. 9). Interestingly, the PL intensity and PLQY showed significantly lower values of

0.7% for the ZnS/GaP thick shells (Supplementary Fig. 10). These results indicate that the strong emission characteristics of GaP originate from the GaP monolayer, and the indirect bandgap characteristics become more pronounced when the GaP layer is thicker than a monolayer.

The influence of ZnS core size on the growth of the GaP shell was investigated by varying the synthesis conditions for ZnS nanocrystals. While the standard ZnS core was synthesized at 260 °C for 60 min, we modified these conditions to produce ZnS core with different diameters (Fig. 2h and Supplementary Fig. 11). The absorption spectra of ZnS/GaP

QSs, as a function of the ZnS core size, reveal two key insights into the structure of ZnS/GaP QSs. First, the position of the absorption shoulder attributed to ZnS remains unaltered following the formation of the GaP shell, suggesting that no additional growth or degradation occurs in the ZnS core (Supplementary Fig. 5). Second, after the formation of the GaP shell, the architecture manifests itself as a core-shell structure composed of ZnS and GaP, respectively, rather than as an alloy[2].

To further verify the heterostructure of the ZnS/GaP QSs, we compared the PL spectra of the ZnS core and the ZnS/GaP QSs. The ZnS core, which was synthesized at 260 °C for 60 min, did not show any PL emissions when excited at 340 nm, however, it showed a PL emission at 336 nm when excited at 280 nm (Supplementary Fig. 12). This ZnS emission remained at the same wavelength in the ZnS/GaP QSs with excitation at 280 nm. This implies that the ZnS/GaP QSs form a heterostructure. Based on these optical properties, we concluded that the ZnS/GaP QSs have a core-shell structure, and that the absorption observed in the 300–390 nm range and the strong PL at 409 nm are solely attributed to the GaP shells. In addition, DFT simulations with 38 different alloying configurations at the ZnS/GaP interface indicated that the core-shell configuration is thermodynamically more stable than the alloy structures, which supports the experimental observations favoring core-shell heterostructures (Supplementary Fig. 13). Particularly, the fast Fourier transform (FFT) of a single ZnS/GaP QS using STEM measurements revealed the distinct crystal structures of ZnS and GaP in different zone axes (Supplementary Fig. 14). These patterns suggest that the ZnS/GaP QSs form a heterostructure rather than a single-phase alloyed structure[39].

To understand the origin of the direct bandgap observed in ZnS/GaP QS, DFT calculations were performed, focusing on the comparisons between GaP-only and ZnS/GaP systems, as shown in Fig. 3a,b. The experimental QS system was modeled using a (110) slab, which was computed as the most stable surface of zinc blende ZnS (Supplementary Table 3). In the DFT simulations, the ZnS core was modeled as an eight-layer slab and the GaP shell was represented by up to six stacked layers on top of the ZnS core to analyze their impact on band diagrams (Supplementary Fig. 15).

The band diagrams of GaP-only and ZnS/GaP systems are comparatively depicted in Fig. 3a, b. In the GaP only systems, the indirect bandgap from Γ to Y was consistently observed regardless of the GaP layer thickness. The bandgap decreased with increasing thickness, which is likely attributed to the change in the degree of quantum confinement effects. On the other hand, in the ZnS/GaP systems, an interesting behavior emerges with the GaP thickness variations. When the number of stacked GaP layers is equal to or less than four, the direct bandgap appears at Γ. However, the bandgap character reverts to the indirect one (from Γ to Y) when the number of GaP layers stacked on the ZnS template exceeds four. This finding identifies the interactions between the ZnS core and a very thin GaP shell as a highly unique strategy enabling the direct band transition. The band diagram results obtained from DFT calculations agree well with experimental observations where the direct band transitions were realized through the use of a ZnS core and the formation of a monolayer-thin GaP shell. Quantitatively, the computed bandgap of the system of a monolayer GaP on the ZnS slab is 3.13 eV, which is very close to our experimental measurement of 3.03 eV. As in the GaP-only case, the bandgap decreased with increasing GaP thickness, reaching the GaP bulk limit.

To further reveal the electronic structural origins of the direct bandgap of the ZnS/GaP systems, atom-projected band diagrams and density-of-states (DOS) are presented in Fig. 3c and Supplementary Fig. 16. The states near VBM were dominantly contributed by the orbitals of the GaP component. On the other hand, the states near CBM were contributed by both ZnS and GaP with comparable strength, leading to the nature of CBM as ZnS-GaP hybrid states. This feature is also visualized in the partial charge density plots of each VBM and CBM state in Fig. 3d, where the charges of CBM state are hybridized from both ZnS and GaP

states. It is important to note that the CBM hybridization is a key factor enabling the direct band transitions occurring in the GaP shell region.

Inspired by these calculations, we conducted more in-depth investigations into the energy structures and corresponding optical transitions in our ZnS/GaP QSs. Figure 4a provides an enlarged view of the absorption spectra of ZnS/GaP QSs, which vary depending on the GaP formation temperature. We observed a series of steps in the absorption spectra of the monolayer GaP shell, featuring consistent peaks at 372 nm (3.3 eV) and 356 nm (3.5 eV). The DFT calculation results revealed that these peaks correspond to the light-hole (lh) to conduction band and heavy-hole (hh) to conduction band transitions, respectively[40,41]. In 2D structures such as quantum wells and quantum shells, the propagation of light is crucial, as it can travel either perpendicular or parallel to the plane. In cases where recombination is driven by lh, light travels parallel to the plane, while recombination driven by hh occurs in a perpendicular direction[41]. As a result, the contribution of recombination by hh is dominant to the PL. Indeed, the PL excitation (PLE) results shown in Fig. 4b suggest that the PLE intensity is highest at 356 nm, corresponding to the hh to conduction band transition, while the shoulder peak at 372 nm, which corresponds to lh recombination, is weaker. The weakest peak at 278 nm is attributed to the indirect bandgap. This energy state analysis can be schematically represented as an energy structure, as depicted in the inset of Fig. 4b, which is consistent with the DFT calculation results in Fig. 3b.

Additionally, unlike typical QDs, where PLE increases as the wavelength decreases, the ZnS/GaP QSs exhibited PLE peaks in the spectrum. This characteristic is consistent with quantum-confined 2D materials[42,43] having discrete energy levels, further corroborating the idea that the GaP shell in this study grows as a monolayer. However, in terms of exhibiting an excitation-independent PL peak, it differs from 2D quantum nanostructures that have intragap states and more closely resembles traditional QDs[34], indicating band-edge emission rather than PL induced by defects or organic matter (Fig. 4c).

To investigate the properties of GaP with and without a ZnS core, we attempted to synthesize GaP dots. Except for the presence of the ZnS core, the same precursor was used for consistency with GaP QS. Due to the extremely small size of the resulting GaP dots, it was practically challenging to achieve both precise purification and size confirmation through TEM analysis[21]. To minimize the influence of byproducts or organic matter, we conducted all analyses after purification. The presence of Ga and P was confirmed through ICP-MS, and the existence of GaP dots was verified through TEM (Supplementary Fig. 17). Figure 4d presents the absorption spectra of GaP dots, and Fig. 4e shows the PLE spectra for the 409 nm emission. Both exhibited peaks at a wavelength of 278 nm, and the graph shapes clearly differed from those of the ZnS/GaP QSs. In particular, the PLE intensity was significantly lower than that of the ZnS/GaP QS, making it difficult to observe the corresponding PL (Fig. 4f). Moreover, when we measured PL by varying the excitation wavelength, the peak shifted, which is unlike the case of the ZnS/GaP QSs. This result indicates that even weak PL is likely attributable to defects or organic substances. These PL trends of ZnS/GaP QSs and GaP dots with different excitation wavelengths were also similarly observed in the film state (Supplementary Fig. 18).

We also conducted experiments using ZnSe as the core material to explore its suitability for the reverse-type I structure (Supplementary Fig. 19). ZnSe/GaP QSs displayed similar trends in both PL and PLE spectra when compared to ZnS/GaP QSs. DFT calculations also demonstrated that GaP grown on ZnSe achieves a direct bandgap. However, in terms of PL intensity, ZnSe/GaP QSs, synthesized under identical conditions (250 °C for 60 min), exhibited only 26% of the PL intensity, underperforming ZnS/GaP QSs (Supplementary Fig. 20). This can be attributed to the larger lattice mismatch (0.07% vs. 3.67%) of ZnSe with GaP[32], which consequently hinders the formation of a high-quality GaP shell, as compared to a ZnS core. As such, it becomes evident that ZnS offers clear advantages in terms of
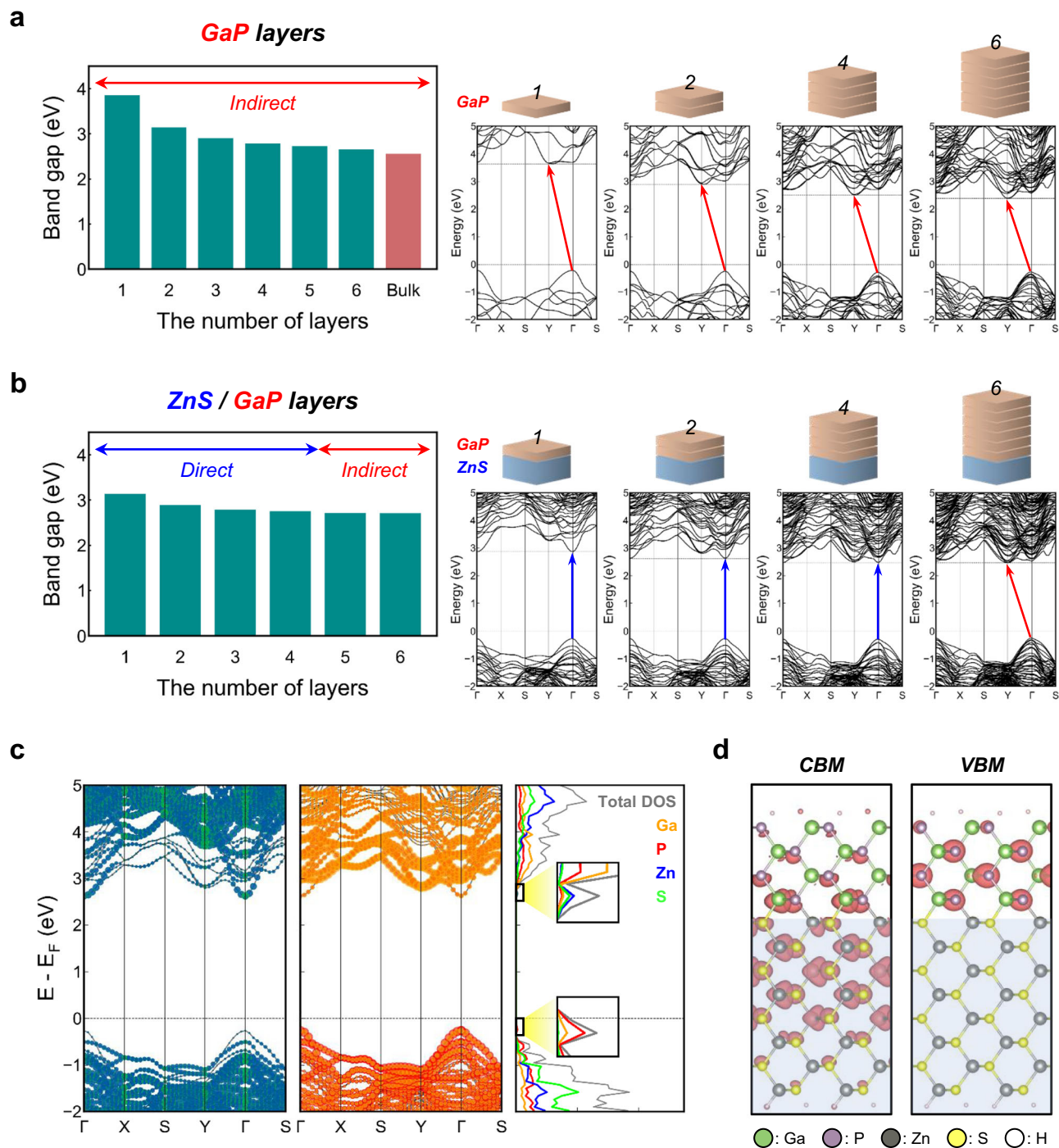
Fig. 3 | DFT-computed band diagrams of GaP only and ZnS/GaP systems.
a Bandgap values and band diagrams of GaP-only and (**b**) ZnS/GaP systems with varying thickness of GaP layers. The experimental QS structure was modeled in a slab geometry, and (110) slabs were selected based on comparisons of surface energy across various planes. **c** Atom-projected band structures and the corresponding DOS data of the ZnS/GaP system with two GaP layers. The size of orange and red circles represents the contributions of Ga and P atoms while that of blue and green circles represents the contributions from Zn and S atoms. **d** Partial charge density plots of the CBM and VBM states of the same system presented in (**c**). The ZnS region is marked with blue shading for a clearer view.

direct bandgap formation for GaP QSs and realizing superior optical performances.

Discussion

We designed and synthesized a ZnS/GaP QS based on the unique energy structure known as the reverse-type I, leading to the successful transformation of the indirect bandgap GaP into a direct bandgap material with substantially improved optical performance. The high PLQY of 45.4% with violet emission clearly demonstrates its direct bandgap nature, presenting an experimental validation of a concept that was previously only theoretical. Our DFT calculations validate the transition to a direct bandgap material for a monolayer-thin GaP on ZnS, which is mainly driven by the formation of hybrid energy states between the two materials at the CBM. This strategy suggests the possibility of broadening the range of III-V compounds as light-emitting materials by demonstrating the direct bandgap transition and band-edge emission of GaP, which previously went unnoticed due to its low optical efficiency. The success of this research has potential
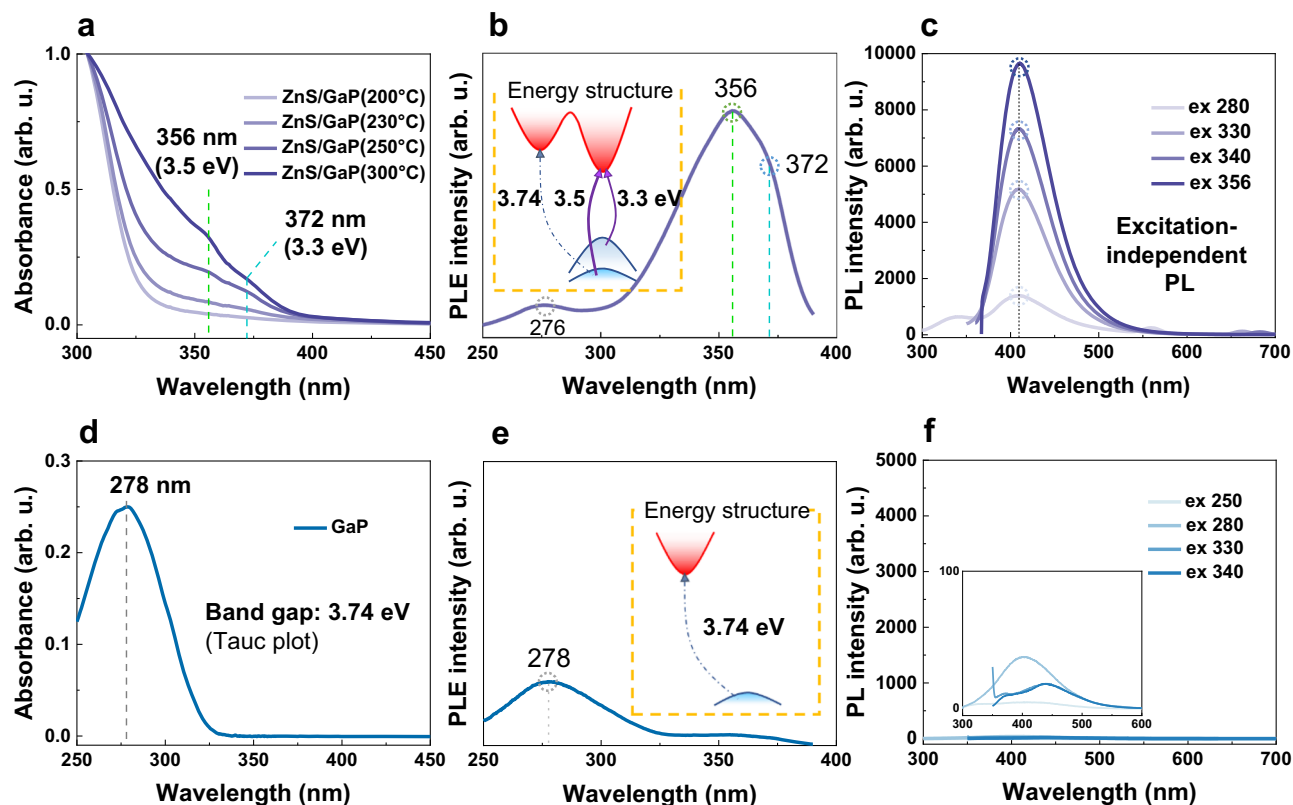
Fig. 4 | Energy structure analysis of ZnS/GaP QSs and GaP dots. a Magnified absorption spectra of ZnS/GaP QSs with the varied synthesis temperature. Absorption steps were observed in the absorption spectra of ZnS/GaP QS. **b** The PL excitation (PLE) spectrum of ZnS/GaP QS synthesized at 250 °C for 60 min, under the condition of 409 nm emission. The inset represents a schematic of the energy structure based on the energies corresponding to each shoulder and peak in the PLE spectrum. **c** The PL spectra of ZnS/GaP QSs synthesized at 250 °C, measured with varying the excitation wavelength. **d** The absorption spectrum of GaP dots and the bandgap measured by a Tauc plot. **e** The PLE spectrum of GaP dots under the condition of 409 nm emission. The inset depicts a schematic of the predicted energy structure of GaP dots. **f** The PL spectra of GaP dots, measured by varying the excitation wavelength. The inset provides a magnified view of the graph. The GaP dots were dispersed in chloroform. Unless otherwise specified, the ZnS cores were synthesized at 260 °C for 60 min, and the default conditions for GaP shell synthesis include a temperature of 250 °C and a synthesis time of 60 min.

implications for optoelectronics, photovoltaic devices, and disease diagnosis and treatment, using more finely-tuned, environmentally safe, and stable light-emitting materials.

Methods

Materials
1-octadecene (ODE, 90%), oleic acid (OA, 90%), zinc acetate (Zn(OAc)$_2$, 99.99%), surfur (S, 99.998%), selenium (Se, 99.99%), chloroform (99.8%), octane (anhydrous, 99%), gallium(III) acetylacetonate (Ga(acac)$_3$, 99.99%) and trioctylphosphine (TOP, 97%) were purchased from Sigma-Aldrich. Acetone (99.5%) and ethanol (99.5%) were purchased from Samchun Chemicals. Gallium chloride (GaCl$_3$, 99.99%) was purchased from Acros Organics. Tris(trimethylsilyl)phosphine ((TMS)$_3$P, 10 wt% in hexane) was purchased from Strem Chemicals.

Preparation of precursor
Firstly, OA and ODE, used for precursor, were degassed at 120 °C for 2 h. A 0.5 M S (or Se)-ODE was prepared by dissolving 0.75 mmol of sulfur (or selenium) powder in 1.5 ml of ODE and stirring it at 400 rpm on a hot plate at 160 °C. A 0.5 M Ga(OA)$_3$/ODE was prepared by combining 0.75 mmol of GaCl$_3$ with 2.25 mmol of OA in 1.5 ml of ODE and stirring it at 400 rpm on an 80 °C hot plate until fully dissolved. 0.5 M (TMS)$_3$P/ODE was prepared by adding 1.25 mmol of (TMS)$_3$P to 2.5 ml of ODE. The mixture was evacuated at room temperature for 1 h to remove hexane and then filled with Ar gas. All the procedures were conducted under an Ar condition to prevent exposure to air.

Synthesis of ZnS/GaP QSs and ZnSe/GaP QSs
In a 50 ml three-neck flask, 1 mmol of Zn(OAc)$_2$ and 0.64 ml of OA were mixed in 9.5 ml of ODE and degassed at 120 °C for 1 h. The temperature was then raised to 300 °C under an Ar flow, followed by the rapid injection of 1 ml of 0.5 M S-ODE. When the temperature dropped to 260 °C, it was maintained for 1 h to synthesize the ZnS core. The reaction vessel subsequently cooled to room temperature, and 2 ml of 0.5 M (TMS)$_3$P/ODE was added. The mixture was evacuated and heated to 110 °C for 20 min. Then, under Ar flow, the temperature was increased to 250 °C, and 1 ml of 0.5 M Ga(OA)$_3$/ODE was slowly injected over a period of 30 min. The shell formation time was expressed by taking 0 min as the moment when the entire amount of precursor required for shell formation has been added. For the sample with a GaP shell formation time of 1 h, the reaction is terminated by cooling to room temperature 1 h after the complete injection of Ga(OA)$_3$/ODE.

After cooling to room temperature, the reaction mixture was subjected to a precipitation step by adding chloroform (6 ml) and acetone (27 ml) to a 3 ml crude solution. This mixture was then centrifuged at 6428 g for 5 min. The resulting precipitate was re-dispersed in chloroform (6 ml) and subjected to a secondary precipitation step by adding ethanol (6 ml) and acetone (12 ml) under the same centrifugation conditions. The collected quantum shells (QS) were dispersed in octane (3 ml) for further analysis.

The synthesis process of ZnSe/GaP QS is identical to that of ZnS/GaP quantum shells, except for the S-ODE injection step. In the S-ODE injection step, S-ODE should be replaced with Se-ODE.

Synthesis of ZnS/GaP thick shells

A 3 ml of as-synthesized ZnS/GaP QSs were purified by mixing with 6 ml of chloroform and 27 ml of acetone, followed by centrifugation (6428 g, 5 min). The precipitated ZnS/GaP QSs were redispersed in 1 ml of toluene.

Next, 3 ml of ODE was prepared in a 3-neck flask and degassed at 120 °C for 1 h, then 1 ml of ZnS/GaP QSs dispersed in toluene was added under the Ar condition. The reaction mixture was evacuated for an additional 15 min to evaporate the toluene, then the temperature was raised to 300 °C under Ar flow and the Ga and P precursors were simultaneously injected over 25 min. The Ga precursor was prepared by degassing 0.25 mmol Ga(acac)$_3$, 0.25 mmol OA, and 0.5 ml ODE at 120 °C for 1 h. The P precursor was prepared by mixing 0.25 mmol (TMS)$_3$P with 0.5 ml TOP in a glove box. After the complete injection of both Ga and P precursors, maintain the reaction for 1 h and then cool the reaction mixture to room temperature.

Synthesis of GaP dots

A total of 4.75 ml of ODE was placed in a 50 ml three-neck flask and evacuated at 120 °C for 1 h. The flask was then cooled to room temperature under Ar condition, and 2 ml of 0.5 M (TMS)$_3$P/ODE was injected. After injection, the mixture was evacuated at 110 °C for 20 min, followed by raising the temperature to 250 °C under an Ar flow. Ga(OA)$_3$/ODE was then injected over a period of 30 min and maintained for 1 h. The heating mantle was removed, and the flask was cooled to room temperature. Toluene (3 ml), acetone (6 ml), and acetonitrile (12 ml) were added to the crude solution (3 ml), followed by centrifugation at 6428 g for 5 min. The precipitate was then dispersed in toluene (2 ml) and subjected to centrifugation with the addition of acetone (8 ml). The obtained GaP dots were dissolved in octane (3 ml) for further analysis.

DFT calculations

DFT calculations were performed using the plane-wave-basis Vienna ab initio simulation package (VASP) code with an energy cutoff of 400 eV[44,45]. The core and valence electrons were treated with the projector-augmented wave method[46]. The generalized gradient approximation was employed to describe the exchange-correlational interactions with the Perdew-Burke-Ernzerhof functional[47]. The ZnS/GaP systems were modeled by the (110) ZnS/GaP slabs with eight atomic layers of ZnS and a vacuum width of 15 Å. The GaP-only systems were also modeled by the (110) slabs with the same vacuum spacing. The surface dangling bonds in our systems were passivated with pseudohydrogen, with properly chosen fractional charges for each species to mimic passivating ligands[48]. The Brillouin zone was sampled with a Γ-centered k-mesh $4 \times 4 \times 1$. The geometry was fully relaxed until the maximum Hellmann−Feynman forces were less than 0.01 eV/Å, and the electronic structures were relaxed with a convergence criterion of 10^{-5} eV. For accurate band structure calculations, we applied PBE-1/2 method, known to well reproduce the band gaps of GaP semiconductor compounds by correcting the electron self-interaction with the Slater half-occupation technique[49,50]. In the PBE-1/2 scheme, a cutoff radius of 3.5 Bohr for P atoms and 3 Bohr for S atoms was employed based on the previously established selection process (Supplementary Fig. 21). The optimized coordinates for all the modeled systems are provided in Supplementary Data 1.

Material characterization

X-ray diffraction patterns were taken by a Rigaku SmartLab High Resolution Powder X-ray diffractometer using a Cu Kα$_1$ source. The scan range was set from 20 ° to 70 ° with a step size of 0.01 ° and a scan rate of 5°/min. UPS measurements were obtained from a Sigma Probe (Thermo VG Scientific) under high vacuum conditions with a He I discharge lamp that generated a photon energy of 21.2 eV. STEM, energy dispersive X-ray mapping, and high-angle annular dark-field (HAADF) STEM images were captured with the FEI Talos F200X microscope,

while TEM analysis was conducted using the JEOL JEM-2011F HR microscope. High-resolution STEM images were obtained with Titan cubed G2 60-300. Both instruments operated at an acceleration voltage of 200 keV. Quantitative analysis was collected using an inductively coupled plasma mass spectrometer (iCAP RQ, Thermo Fisher Scientific) and inductively coupled plasma optical emission spectroscopy (ICP-OES 720, Agilent). The pre-treatment involved microwave reaction at 200 °C for 30 min under a mixture of 70% HNO$_3$ (7 ml) and 35% HCl (3 ml). The absorption and PL measurements were carried out using an ultraviolet-visible spectrometer (Shimadzu UV-1800) and fluorescence spectrophotometer (Hitachi F7000), respectively. PLQY was measured using an absolute photoluminescence quantum yield spectrometer (Quantaurus-QY Plus, Hamamatsu). The absorption, PL, and PLQY measurements were all performed in the solution state, with the nanocrystals (ZnS core, ZnS/GaP QS, or GaP dot) dispersed in octane.

Reporting summary

Further information on research design is available in the Nature Portfolio Reporting Summary linked to this article.

Data availability

The data that support the findings of this study are available from the corresponding author upon request. Data can only be shared for non-commercial academic purposes and will require a data user agreement.

References

1. Cassabois, G., Valvin, P. & Gil, B. Hexagonal boron nitride is an indirect bandgap semiconductor. *Nat. Photon.* **10**, 262–266 (2016).
2. Fadaly, E. M. T. et al. Direct-bandgap emission from hexagonal Ge and SiGe alloys. *Nature* **580**, 205–209 (2020).
3. Wilson, D. J. et al. Integrated gallium phosphide nonlinear photonics. *Nat. Photon.* **14**, 57–62 (2020).
4. Healy, N. et al. Extreme electronic bandgap modification in laser-crystallized silicon optical fibres. *Nat. Mater.* **13**, 1122–1127 (2014).
5. Mak, K. F., Lee, C., Hone, J., Shan, J. & Heinz, T. F. Atomically thin MoS$_2$: a new direct-gap semiconductor. *Phys. Rev. Lett.* **105**, 136805 (2010).
6. Zeng, M. et al. Bandgap tuning of two-dimensional materials by sphere diameter engineering. *Nat. Mater.* **19**, 528–533 (2020).
7. Dang, C. et al. Achieving large uniform tensile elasticity in micro-fabricated diamond. *Science* **371**, 76–78 (2021).
8. Ning, C.-Z., Dou, L. & Yang, P. Bandgap engineering in semi-conductor alloy nanomaterials with widely tunable compositions. *Nat. Rev. Mater.* **2**, 17070 (2017).
9. Gupta, A. et al. Composition-defined optical properties and the direct-to-indirect transition in core–shell In$_{1−x}$Ga$_x$P/ZnS colloidal quantum dots. *J. Am. Chem. Soc.* **145**, 16429–16448 (2023).
10. Kim, J. M. et al. Strain Engineering of Low-Dimensional Materials for Emerging Quantum Phenomena and Functionalities. *Adv. Mater.* **35**, 2107362 (2023).
11. Behrman, K. & Kymissis, I. Micro light-emitting diodes. *Nat. Electron.* **5**, 564–573 (2022).
12. Califano, M., Lu, R. & Zhou, Y. Indirect to direct band gap transformation by surface engineering in semiconductor nanostructures. *ACS Nano* **15**, 20181–20191 (2021).
13. Won, R. Integrating silicon photonics. *Nat. Photon.* **4**, 498–499 (2010).
14. Kim, Y.-H., Jun, Y.-W., Jun, B.-H., Lee, S.-M. & Cheon, J. Sterically induced shape and crystalline phase control of GaP nanocrystals. *J. Am. Chem. Soc.* **124**, 13656–13657 (2002).
15. Mićić, O. I. et al. Synthesis and Characterization of InP, GaP, and GaInP$_2$ Quantum Dots. *J. Phys. Chem.* **99**, 7754–7759 (1995).
16. Assali, S. et al. Direct band gap wurtzite gallium phosphide nano-wires. *Nano Lett.* **13**, 1559–1563 (2013).
17. Kim, S. et al. Origin of photoluminescence from colloidal gallium phosphide nanocrystals synthesized via a hot-injection method. *RSC Adv.* **5**, 2466–2469 (2015).

18. Choi, Y., Choi, C., Bae, J., Park, J. & Shin, K. Synthesis of gallium phosphide quantum dots with high photoluminescence quantum yield and their application as color converters for LEDs. *J. Ind. Eng. Chem*. **123**, 509–516 (2023).

19. Furis, M. et al. Surfactant-imposed interference in the optical characterization of GaP nanocrystals. *J. Phys. Chem. B* **107**, 11622–11625 (2003).

20. Zhang, H. et al. High-efficiency green InP quantum dot-based electroluminescent device comprising thick-shell quantum dots. *Adv. Opt. Mater*. **7**, 1801602 (2019).

21. Kim, K.-H. et al. Cation-exchange-derived InGaP alloy quantum dots toward blue emissivity. *Chem. Mater*. **32**, 3537–3544 (2020).

22. Gagliano, L. et al. Pseudodirect to direct compositional crossover in wurtzite GaP/In$_x$Ga$_{1-x}$P core–shell nanowires. *Nano Lett*. **16**, 7930–7936 (2016).

23. De, A. & Pryor, C. E. Predicted band structures of III-V semiconductors in the wurtzite phase. *Phys. Rev. B* **81**, 155210 (2010).

24. Belabbes, A., Panse, C., Furthmüller, J. & Bechstedt, F. Electronic bands of III-V semiconductor polytypes and their alignment. *Phys. Rev. B* **86**, 075208 (2012).

25. Pu, C. & Peng, X. To battle surface traps on CdSe/CdS core/shell nanocrystals: shell isolation versus surface treatment. *J. Am. Chem. Soc*. **138**, 8134–8142 (2016).

26. Lei, H., Li, J., Kong, X., Wang, L. & Peng, X. Toward surface chemistry of semiconductor nanocrystals at an atomic-molecular level. *Acc. Chem. Res*. **56**, 1966–1977 (2023).

27. Ding, Y. et al. Efficient full-color boron nitride quantum dots for thermostable flexible displays. *ACS Nano* **15**, 14610–14617 (2021).

28. Rakshit, S., Cohen, B., Gutiérrez, M., El-Ballouli, Aa. O. & Douhal, A. Deep blue and highly emissive ZnS-passivated InP QDs: facile synthesis, characterization, and deciphering of their ultrafast-to-slow photodynamics. *ACS Appl. Mater. Interfaces* **15**, 3099–3111 (2023).

29. Li, S.-N. et al. Electroluminescence from GaN-Based Quantum Dots. *Adv. Opt. Mater*. **12**, 2301427 (2024).

30. Cho, W., Zhou, Z., Lin, R., Ondry, J. C. & Talapin, D. V. Synthesis of colloidal GaN and AlN nanocrystals in biphasic molten salt/organic solvent mixtures under high-pressure ammonia. *ACS Nano* **17**, 1315–1326 (2023).

31. Choi, Y. C. et al. Blue emission of α-GaN colloidal quantum dots via Zn doping. *Chem. Mater*. **31**, 5370–5375 (2019).

32. Tamang, S., Lincheneau, C., Hermans, Y., Jeong, S. & Reiss, P. Chemistry of InP nanocrystal syntheses. *Chem. Mater*. **28**, 2491–2506 (2016).

33. Liang, X. et al. constructing a z-scheme heterojunction photocatalyst of GaPO$_4$/α-MoC/Ga$_2$O$_3$ without mingling type-II heterojunction for CO$_2$ reduction to CO. *ACS Appl. Mater. Interfaces* **13**, 33034–33044 (2021).

34. Won, Y.-H. et al. Highly efficient and stable InP/ZnSe/ZnS quantum dot light-emitting diodes. *Nature* **575**, 634–638 (2019).

35. Syed, N. et al. Printing two-dimensional gallium phosphate out of liquid metal. *Nat. Commun*. **9**, 3618 (2018).

36. Ren, M. et al. Band structures in silicene on monolayer gallium phosphide substrate. *Solid State Commun*. **239**, 32–36 (2016).

37. Wang, T., Farvid, S. S., Abulikemu, M. & Radovanovic, P. V. Size-tunable phosphorescence in colloidal metastable γ-Ga$_2$O$_3$ nanocrystals. *J. Am. Chem. Soc*. **132**, 9250–9252 (2010).

38. Bennett, E. et al. Size Dependent Optical Properties and Structure of ZnS Nanocrystals Prepared from a Library of Thioureas. *Chem. Mater*. **34**, 706–717 (2022).

39. Zhou, N. et al. P-GaSe/N-MoS$_2$ Vertical Heterostructures Synthesized by van der Waals Epitaxy for Photoresponse Modulation. *Small* **14**, 1702731 (2018).

40. Ithurria, S. & Dubertret, B. Quasi 2D colloidal CdSe platelets with thicknesses controlled at the atomic level. *J. Am. Chem. Soc*. **130**, 16504–16505 (2008).

41. David, A. & Miller, B. Optical physics of quantum wells in *Quantum Dynamic of Simple Systems*. 239-266 (CRC Press, 1996).

42. Zhang, Q., Wang, R., Feng, B., Zhong, X. & Ostrikov, K. Photoluminescence mechanism of carbon dots: triggering high-color-purity red fluorescence emission through edge amino protonation. *Nat. Commun*. **12**, 6856 (2021).

43. Liu, F. et al. Fluorescent carbon- and oxygen-doped hexagonal boron nitride powders as printing ink for anticounterfeit applications. *Adv. Opt. Mater*. **7**, 1901380 (2019).

44. Kresse, G. & Furthmüller, J. Efficient iterative schemes for ab initio total-energy calculations using a plane-wave basis set. *Phys. Rev. B* **54**, 11169–11186 (1996).

45. Kresse, G. & Joubert, D. From ultrasoft pseudopotentials to the projector augmented-wave method. *Phys. Rev. B* **59**, 1758–1775 (1999).

46. Blöchl, P. E. Projector augmented-wave method. *Phys. Rev. B* **50**, 17953–17979 (1994).

47. Perdew, J. P., Burke, K. & Ernzerhof, M. Generalized gradient approximation made simple. *Phys. Rev. Lett*. **77**, 3865–3868 (1996).

48. Deng, H.-X., Li, S.-S., Li, J. & Wei, S.-H. Effect of hydrogen passivation on the electronic structure of ionic semiconductor nanostructures. *Phys. Rev. B* **85**, 195328 (2012).

49. Ferreira, L. G., Marques, M. & Teles, L. K. Approximation to density functional theory for the calculation of band gaps of semiconductors. *Phys. Rev. B* **78**, 125116 (2008).

50. Ferreira, L. G., Marques, M. & Teles, L. K. Slater half-occupation technique revisited: the LDA-1/2 and GGA-1/2 approaches for atomic ionization energies and band gaps in semiconductors. *AIP Adv*. **1**, 032119 (2011).

Acknowledgements

Author contributions

H.S. and Y.S.J. conceived the study. H.S. performed the experiments and analyzed the data. D.H. and D.K. performed the DFT calculations. H.C. contributed to the analysis and synthesis method. H.J. obtained the high-resolution STEM image. H.C., G.Y.K., and K.M.S. contributed the discussion. H.S., D.H., M.-J.C., D.K., and Y.S.J wrote the manuscript.

Competing interests

The authors declare no competing interests.

Additional information

Supplementary information The online version contains supplementary material available at https://doi.org/10.1038/s41467-024-52535-8.

Correspondence and requests for materials should be addressed to Min-Jae Choi, Donghun Kim or Yeon Sik Jung.

Peer review information *Nature Communications* thanks Jongnam Park and the other, anonymous, reviewer(s) for their contribution to the peer review of this work. A peer review file is available.

Reprints and permissions information is available at http://www.nature.com/reprints